Chemical disorder as an engineering tool for spin polarization in Mn₃Ga-based Heusler systems

S. Chadov, S. W. D'Souza, L. Wollmann, J. Kiss, G. H. Fecher, and C. Felser

Max-Planck-Institut für Chemische Physik fester Stoffe, 01187 Dresden, Germany

Our study highlights spin-polarization mechanisms in metals by focusing on the mobilities of conducting electrons with different spins instead of their quantities. Here, we engineer electron mobility by applying chemical disorder induced by nonstoichiometric variations. As a practical example, we discuss the scheme that establishes such variations in tetragonal Mn₃Ga Heusler material. We justify this approach using first-principles calculations of the spin-projected conductivity components based on the Kubo-Greenwood formalism. It follows that, in the majority of cases, even a small substitution of some other transition element instead of Mn may lead to a substantial increase in spin polarization along the tetragonal axis.

I. INTRODUCTION

An improved understanding of the influence of disorder in solids yields potential new approaches to the state-of-the-art design of multicomponent materials. Despite the popular view that disorder should be avoided by any means, one can find its constructive influence on physical properties in various applied fields. Examples include the disorder-induced mechanical work hardening of materials [1], "softer" examples such as the efficient blocking of sound waves in liquid foams [2], and the Anderson localization of light in disordered photonic crystals [3]. By carefully reviewing the literature, one finds many more constructive examples. Constructive disorder simply prevents the propagation of certain quasiparticles. Indeed, in the first example, mechanical dislocations are blocked by other types of random defects; in the second, ultrasonic phonons are blocked by random foam bubbles; and in the third, electromagnetic waves are blocked by the breaking of the translational symmetry in the photonic crystal. Of course, similar phenomena also accompany electronic propagation in metals, where the breaking of translational symmetry (static or dynamic) leads to a nonzero resistivity. Here, one of the most dramatic examples is the Anderson localization [4,5], which completely blocks the propagation of an electron despite the absence of a semiconducting gap in the density of states. This can have constructive implications. For example, it was recently proposed that Anderson localization induced in topologically nontrivial systems, such as HgTe-type semimetals, should result in a new class of topological insulator [6–8]. On the other hand, in "typical" metals (i.e., systems with a conducting electron density of $n_F \gtrsim 5 \times 10^{22}$ cm^{-3}), the Anderson-Mott criterion [9] ($a_B n_F^{1/3} < 0.25$, where a_B is the Bohr radius) cannot be fulfilled, so an unlimited increase in disorder leads to a saturation of metallic resistivity, which, in practice, is restricted by the empirical Mooij limit, $\rho_{max} \lesssim 300$ $\mu\Omega$ cm [10].

Here, we would like to demonstrate another interesting effect that can be induced by disorder in metallic systems, the so-called *spin-selective* electron localization. Specifically, we will justify the possibility of creating such a type of disorder, which noticeably localizes the conducting electrons of one spin but almost negligibly affects the conduction of the other spin. It is rather clear that, since the spin subbands in a magnetic metal are different, their conductivities also differ (i.e., $\sigma^\uparrow \neq \sigma^\downarrow$).

The extreme case, which is especially interesting in terms of spintronics, is the half-metallicity (i.e., $\sigma^\uparrow > 0$, $\sigma^\downarrow = 0$ or vice versa) characterized by the highest possible amplitude of the spin polarization, $P = \frac{\sigma^\uparrow - \sigma^\downarrow}{\sigma^\uparrow + \sigma^\downarrow} = \pm 1$. It can be realized in the special class of materials known as half-metals [11,12], which possess a semiconducting band gap in one spin channel only (i.e., $n_F^\downarrow = 0$, $n_F^\uparrow > 0$ or vice versa). However, as one can see in the simple Drude picture, $\sigma \sim n_F l$. Thus, the conductivity also scales with an electronic mean free path l, providing the potential for $P = \frac{n_F^\uparrow l^\uparrow - n_F^\downarrow l^\downarrow}{n_F^\uparrow l^\uparrow + n_F^\downarrow l^\downarrow}$, to be adjusted by manipulation of the electron mobilities, $l^{\uparrow(\downarrow)}$, in different spin channels rather than adjusting the $n_F^{\uparrow(\downarrow)}$ only.

A large number of mechanisms exist that favor disorder in solids provided by a diverse manifold of the degrees of freedom, whether thermal (such as phonons, magnons, polarons) or fully intrinsic (such as through geometrical frustration, stoichiometric variations, and electron interaction). To engineer such mechanisms efficiently, one must understand their impact on the electronic structure. At present, certain connections can be established using special mean-field theories [e.g., the coherent potential approximation (CPA) [13–15] or dynamical mean-field theory (DMFT) [16–20]], statistical methods (e.g., Monte-Carlo-based simulations), or combined approaches.

Here, we will restrict our engineering to a very fundamental level by improving the ground-state electronic transport characteristics through a particular type of chemical disorder, as it is one of the most common phenomena in polyatomic solid compositions. The simplest way to introduce chemical disorder is through variation of the stoichiometry. Here, a convenient test environment is provided by the Heusler family of materials, which typically have a ternary composition: two different transition metals (TMs) and one main-group element (MG). The majority of these substances crystallize in the fcc-based cubic structure (centrosymmetric Fm-$3m$ or noncentrosymmetric F-$43m$) and obey the same chemical ordering rules [21]. By substituting one TM for another TM or one MG by another MG, the properties of Heusler materials can be varied widely without affecting their structure, from nonmagnetic/semiconducting to magnetic/metallic. In particular, the latter class includes the majority of the known half-metals as given in Refs. [11,12]. A nonstoichiometric substitution will lead to a random occupation of the

corresponding Wyckoff sites by automatically breaking the translational invariance. This random site occupation by two or more elements with localized electronic subbands (e.g., $3d$ states) centered at different energies will disturb the coherent scattering of the delocalized (mobile) electrons at corresponding energies and result in their partial localization. Thus, if the nonstoichiometric substitution induces these random fluctuations within the energy window containing the Fermi level (E_F), the resistivity will increase. The concept is therefore clear; we must create such an energy window at E_F in one spin channel, and simultaneously shift it away from E_F in the other channel. Such a situation can be maintained, obviously, only in magnetic systems.

II. RANDOM FLUCTUATION DESIGN: Mn₃Ga AND ITS DERIVATIVES

We select Mn_3Ga Heusler as a suitable object, since it possesses strong local moments and it is not a half-metal. This is because of its tetragonal distortion, which reduces its point symmetry to $I4/mmm$. Chemically speaking it is a binary, however it contains two types of Mn in the $2a$ and $4c$ Wyckoff positions [marked red and blue, respectively, in Fig. 1(a)] that differ by their nearest-neighbor environment. Mn($2a$) has the largest local moment (according to different measurements and first-principles estimations ≈ 3–$4\mu_B$) coupled antiparallel to Mn($4c$), which has a smaller moment of ≈ 2–$3\mu_B$. Since the $4c$ class contains two Mn atoms (in $2c$ and $2d$, which are equivalent), the total magnetization, M, is oriented along the $4c$ local moments. $M \approx 1.7\mu_B$/f.u. (f.u. denotes formula unit) according to the first-principles calculation (see, e.g., [22]), and $M \approx 1.1\mu_B$/f.u. according to experiment [23–25] (note that the saturation was not achieved).

Let us examine the energetic structures of our future scattering centers (localized $3d$ states of Mn). They are shown schematically in Fig. 1(a). Mn($2a$), which exhibits the strongest magnetic moment, is close to the half-filled state. Its $3d$ shell contains five spin-down electrons, whereas the spin-up states are empty (ideally this should result in $5\mu_B$, however this can differ in calculations since the amplitude of the local moment depends on the position at which the "border" between the atoms is set). On the other hand, Mn($4c$) exhibits a smaller moment and weaker exchange split; this simply means that, whereas the spin-up band is fully filled, the spin-down band is not fully empty, i.e., it contains E_F. Such a "half-metallic" structure of the localized electronic subsystem (the delocalized s and p conducting electrons, which are not shown in the scheme, do not have a band gap in any of the spin channels) fits well into the framework of the Anderson impurity model [26], which explains the spin dependence of the conducting electron scattering on a given magnetic impurity. In the second-order perturbation theory, the scattering process involves an intermediate state in which a conducting electron occupies an impurity level. At E_F, this is a partially filled spin-down $3d$ subband of Mn($4c$). According to the Pauli exclusion principle, intermediate states in which the impurity level is occupied by two electrons with the same spin orientation are forbidden. Thus, the spin-down conducting electrons will be repelled from the Mn($4c$) spin-down subband more strongly, which results in a relative increase in the
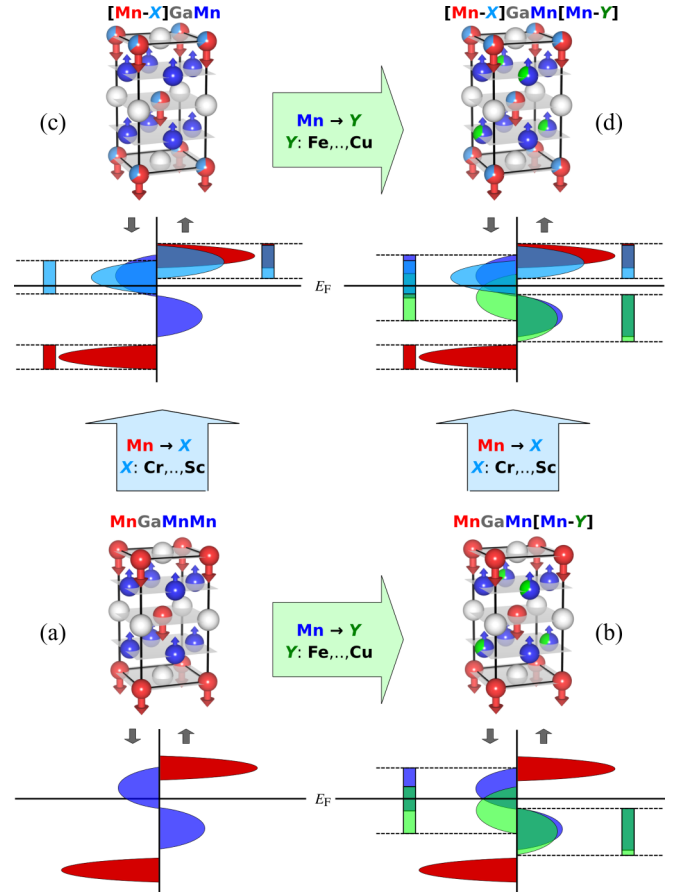

FIG. 1. (Color online) (a) Mn_3Ga unit cell: Mn atoms in the $2a$ (red) and $2c/2d = 4c$ (blue) Wyckoff sites; Ga atoms are in $2b$ (gray); arrows indicate atomic magnetic moments. According to the sequence of Wyckoff positions, $2a\,2b\,2c\,2d$, we label this compound as MnGaMnMn. (b) Substituting a late TM in place of Mn (Y, light green) results in a MnGaMn[Mn-Y] alloy with Mn-Y disorder on $2d$ sites. (c) Replacing Mn with an early TM (X, light blue) results in a [Mn-X]GaMnMn alloy with Mn-X disorder on $2a$. (d) Simultaneous combination of (b) and (c): [Mn-X]GaMn[Mn-Y]. The corresponding spin-projected and atomic-resolved $3d$-DOS scheme for each prototype system (left-oriented peaks are spin-down, right-oriented are spin-up, as indicated by gray arrows). The atom-projected DOS contributions obey the same color code as that used for the atoms; vertical colored bars indicate the energy windows in which the electronic levels randomly fluctuate.

spin-down resistivity component, $\rho^\downarrow$. The only ingredient that is still missing is the chemical disorder on the $4c$ sites, which leads to a random fluctuation of the spin-down localized d-electron subband by causing it to become an efficient scattering center.

This type of disorder can be introduced by substituting some other TM in place of Mn. One of the general rules that holds quite unambiguously for Heusler alloys concerns their chemical ordering (see, e.g., [21]; several total energy comparisons based on the first principles are presented in Sec. A). Specifically, the *earliest* TM (which is located closer to the left side of the Periodic Table, i.e., it belongs to the earliest group) shares the same atomic layer as the MG element (e.g., if Ga occupies $2b$, the earliest TM occupies the $2a$

Wyckoff site). Thus, for Mn-Y substitution with the *later* TMs, $Y =$ Fe, Co, Ni, Cu, the earliest TM is Mn, which therefore remains in $2a$. For this reason, Y will randomly occupy the $4c$ Wyckoff sites. As follows from the present calculations (in the case of $Y =$ Fe, Co, Ni it is also known experimentally [23,24]), such substitution preferably occurs on one of the two $4c$ sites ($2c$ or $2d$; here, let us choose $2d$) by rendering them nonequivalent [see Fig. 1(b)]. According to the sequence $2a$ $2b$ $2c$ $2d$, we label the resulting compound MnGaMn[Mn$_{1-y}Y_y$]. Statistically, its point symmetry reduces from $I4/mmm$ to I-$4m2$ (no inversion). Due to the similarity with Mn($2c/2d$), the magnetic moments of $Y(2d)$ are coupled negatively to Mn($2a$), i.e., they are oriented up. Since $Y(2d)$ has a smaller magnetic moment compared to Mn($2c/2d$) (because of its more complete d shell), its partially occupied spin-down subband is downshifted energetically with respect to Mn($2c/2d$), whereas its fully occupied spin-up subband is centered below E_F, similar to the spin-up subband of Mn($2c/2d$). It is clear that such substitution yields the spin-down random fluctuation window including E_F, whereas the spin-up window is situated below E_F [see Fig. 1(b)].

A similar effect can be maintained by replacing Mn with earlier TMs: $X =$ Cr, V, Ti, and Sc. According to the aforementioned chemical ordering rules, the earlier TMs occupy the $2a$ Wyckoff site, which is represented in formal notation as [Mn$_{1-x}X_x$]GaMnMn [see Fig. 1(c)]. This does not change the $I4/mmm$ point symmetry. Because of the similarity with Mn($2a$), the magnetic moments of $X(2a)$ are also coupled negatively to Mn($4c$), i.e., they are down-oriented. Since the d shell of the X element is less than half-filled, its spin-up subband is fully empty (it is situated above E_F), whereas the spin-down subband is partially filled (contains E_F). This again provides two randomly fluctuating energy windows: one including E_F in the spin-down channel, and the other one above E_F in the spin-up channel. An additional energy regime of random fluctuations that occurs in the spin-down channel relatively far below E_F exists, which is caused by the deepest fluctuating spin-down subband of Mn($2a$), as shown in Fig. 1(c). Since both substitutions [Mn$_{1-x}X_x$]GaMnMn and MnGaMn[Mn$_{1-y}Y_y$] are independent, they can be simultaneously combined into [Mn$_{1-x}X_x$]GaMn[Mn$_{1-y}Y_y$], as shown in Fig. 1(d). The resulting compound statistically corresponds to the lowest I-$4m2$ symmetry, and its fluctuation spectrum represents a superposition of the energy windows in cases (b) and (c).

III. FIRST-PRINCIPLES JUSTIFICATION

A. Technical details

All the present computations were performed using the fully relativistic SPR-KKR (spin-polarized relativistic Korringa-Kohn-Rostoker) Green's function method [27], using the generalized gradient approximation (GGA) in a form proposed by Perdew, Burke, and Ernzerhof (PBE) [28]. The wavefunction basis is constructed using the relativistic solutions in the spherical potential up to $l = 3$ harmonics; 824 and 10^6 k vectors were used to sample the irreducible part of the Brillouin zone during the self-consistent cycle and for the subsequent calculations of residual resistivities, respectively

(see Secs. III B and III D). To treat all the systems on an equal footing, in all cases the most general point group symmetry I-$4m2$ was assumed. Numerical accuracy for the total energies is set to 10^{-8} Ry/f.u..

The chemical disorder was treated within the CPA [13–15], as implemented in SPR-KKR. The electronic structure is represented via the Bloch spectral function (BSF), defined as a Fourier transform of the real-space Green's function $G(\vec{r}, \vec{r}\,', E)$ with

$$A(\vec{k}, E) = -\frac{1}{\pi N} \operatorname{Im} \sum_{n,m=1}^{N} e^{i\vec{k}(\vec{R}_n - \vec{R}_m)}$$

$$\times \int d^3 r \langle G(\vec{r} + \vec{R}_n, \vec{r} + \vec{R}_m, E) \rangle,$$

where $\langle\rangle$ is the CPA average and $\vec{R}_{n,m}$ are the atomic site coordinates. $A(\vec{k}, E)$ can be interpreted as a $\vec{k}$-resolved DOS function, since

$$n(E) = \frac{1}{\Omega_{BZ}} \int_{\Omega_{BZ}} d^3 k \, A(\vec{k}, E),$$

with $n(E)$ indicating the total DOS function, and Ω_{BZ} is the Brillouin zone volume.

B. Assumptions and limitations

Since we want to figure out the general trends of transport characteristics, by following the idea proposed in Sec. II we are going to treat many systems on an equal footing. Since most of them were not reported experimentally, we need to make reasonable assumptions concerning their crystal structure, chemical order, and magnetic order, as it is impossible to optimize all these degrees of freedom simultaneously. Moreover, since the numerical models used in *ab initio* methods are approximate anyway, there is no guarantee that the result obtained within such a resource-demanding procedure will be physically reasonable, despite the fact that it can be fully correct. Thus, our main assumptions are the following: (i) We assume all the systems have the same crystal parameters as the tetragonal phase of Mn$_3$Ga. Several experimental results [23,24] demonstrate that the structural parameters of these tetragonal phases are indeed quite close: For example, for Mn$_3$Ga: $a = 3.9$ Å, $c/a = 1.81$; Mn$_{2.7}$Co$_{0.3}$Ga: $a = 3.874$ Å, $c/a = 1.84$; Mn$_{2.8}$Fe$_{0.2}$Ga: $a = 3.874$ Å, $c/a = 1.83$. (ii) We assume the chemical ordering follows the rules discussed in Sec. II. Despite the absence of a general physical explanation, almost all the experimentally known Heusler materials (cubic or tetragonally distorted) follow these rules quite unambiguously. In addition, in Sec. A we show a few examples of the total energy comparison that validate these rules. (iii) All the local magnetic moments are assumed to be collinear. Indeed, for the group of Heusler materials based on Mn and Ga, the noncollinear order has not been reported yet. Second, our own calculations for the Mn$_3$Ga parent compound (not shown here), using the PY-LMTO package [29] as well as the SPR-KKR, do not indicate that this system is proximate to the noncollinear state. Among the tetragonal Mn-containing Heusler systems, the strong canting of local moments was indicated theoretically and confirmed experimentally so far only for Mn$_2$RhSn, Mn$_2$IrSn, and Mn$_2$PtIn [30]. As follows from the theoretical

analysis, the noncollinear order in these systems is caused by the additional antiparallel coupling between the second nearest Mn-containing atomic (001) planes, which crucially depend on the type of MG atom (Sn or In).

It is clear that the lower the substitution rate is (x or y), the less probable (or less noticeable) would be the unexpected structural or electronic changes, and thus the assumptions (i)–(iii) gain more validity. For this reason, among all the cases considered here, the practically interesting examples are those in which the substitution rate does not exceed 10–20 % ($0 < x, y \lesssim 0.2$). Nevertheless, since it is interesting to also track the spin polarization at the disorder rate maximum, we will study $Mn_{3-y}Y_yGa$ and $Mn_{3-x}X_xGa$ within a wide range ($0 \leqslant x, y \leqslant 0.5$). To examine the effects of the combined substitution (in $Mn_{3-x-y}X_xY_yGa$), we will ensure for consistency that the sum of these rates does not exceed the maximal rate ($x = y, x + y \leqslant 0.5$).

The use of the CPA alloy theory means that we assume the Mn-X or Mn-Y interchange occurs equirandomly; it is clear that in this case, the short-range-order effects, caused by a particular type of the nearest atomic environment, are not described properly, such as chemical segregation or relaxation of the structure around the impurity. On the other hand, the CPA still remains the only practical technique, which reproduces from first principles the most essential properties of

disorder, such as the energy-dependent shifts and broadening of the electronic states, although they are approximate. In turn, these properties are necessary for further calculations of the linear-response transport coefficients.

The scheme, which is used to calculate the residual resistivities, is based on the Kubo-Greenwood linear-response formalism [31,32]. In this case, the ensemble average of the two-particle Green's function is approximated by the product of the two one-particle averaged Green's functions, delivered by the CPA. To check the significance of this assumption, we have taken into account the so-called vertex corrections [33], which change the bare result by 1% of its magnitude at most.

C. Visual analysis of the Bloch spectral function

By comparing the calculated spin-projected Bloch spectral function (BSF) (red and blue indicate spin-up and spin-down, respectively) of Mn_3Ga [Fig. 2(a)] with $Mn_{2.5}Co_{0.5}Ga$ [Fig. 2(b)] and $Mn_{2.5}V_{0.5}Ga$ [Fig. 2(c)], one can identify all the fluctuation regimes (visualized as broadened regions) schematically presented in Fig. 1. In the case of Mn-Co substitution, the random fluctuations in the spin-down channel span a wide energy window $\approx E_F \pm 2$ eV, whereas no broadening is observed for the spin-up states crossing E_F, as the spin-up fluctuations begin only at 1 eV below E_F. In the case of Mn-V,
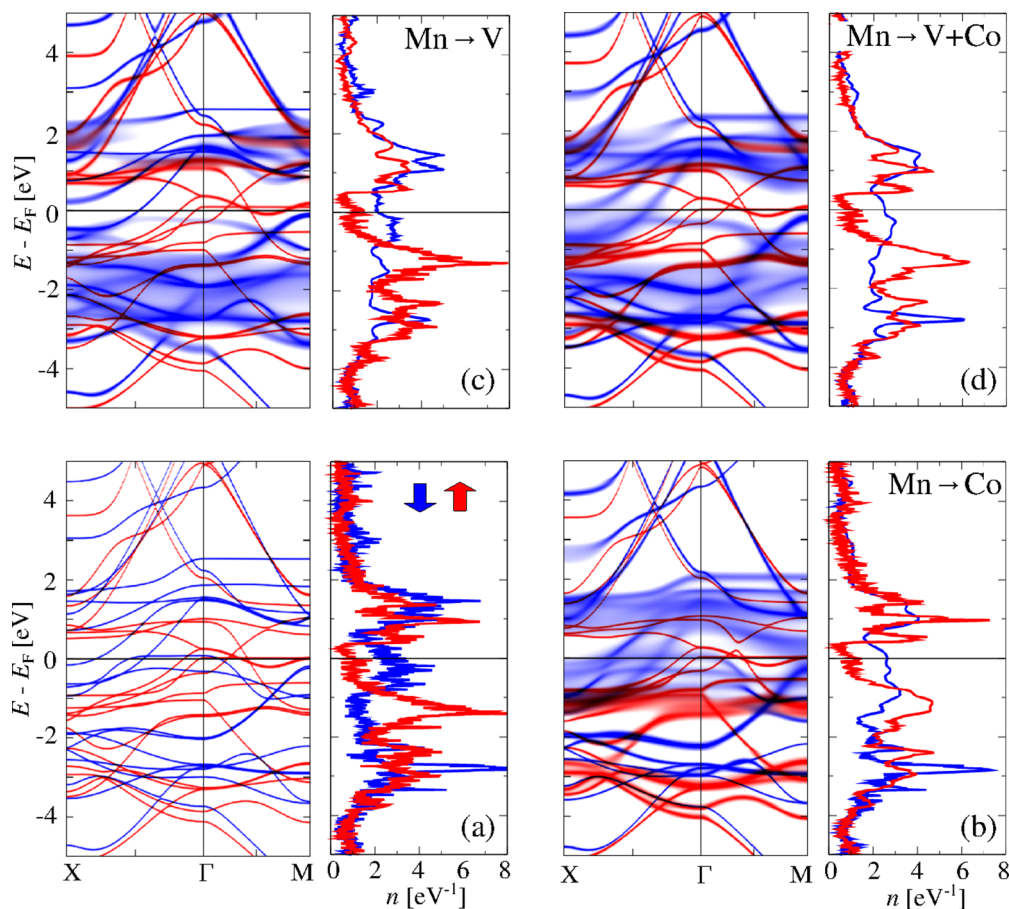

FIG. 2. (Color online) Spin-projected BSF (red and blue indicate spin-up and spin-down, respectively) along the X-Γ-M path and the spin-projected total DOS computed for (a) MnGaMnMn, (b) MnGaMn[$Mn_{0.5}Co_{0.5}$], (c) [$Mn_{0.5}V_{0.5}$]GaMnMn, and (d) [$Mn_{0.25}V_{0.25}$]GaMn[$Mn_{0.25}Co_{0.25}$], corresponding to the schemes in Figs. 1(a), 1(b), 1(c), and 1(d), respectively.

the spin-down fluctuation region is even wider: it roughly spans the -3.5 to 2 eV range as a fluctuating superposition of the lower and higher bands of Mn(2a) and V(2a), respectively. Again, almost no broadening of the spin-up states is observed at E_F, as the spin-up fluctuation window is now shifted above E_F (from 0.5 to 2 eV). In the combined $Mn_{2.5}V_{0.25}Co_{0.25}Ga$ case [Fig. 2(d)], the fluctuation regime clearly represents a superposition of the fluctuation energy windows in Figs. 2(c) and 2(d).

Before we examine the quantitative estimates, it is instructive to note the difference in informational content provided by the BSF and DOS. In all cases, the spin-resolved DOS indicates that at E_F, $n_F^\uparrow < n_F^\downarrow$, which may lead us to naively assume a negative spin polarization, i.e., $P \sim n_F^\uparrow - n_F^\downarrow < 0$. Such an estimate is used quite often, even today. In certain cases, this estimate can be improved upon if, instead of the total DOS, only its s- and p-electron projections are considered, but even such an improvement can be efficient only when the electron mobility values in both spin channels are close. In contrast, we see from the BSFs that the electron momentum uncertainties ($\Delta k \sim l^{-1}$) at E_F produced by disorder are also very different for the two spins ($\Delta k^\uparrow < \Delta k^\downarrow$) and suggest the opposite conclusion, i.e., a positive spin polarization, $P \sim l^\uparrow - l^\downarrow > 0$. Obviously, in such situations, a final conclusion can be made only if it is based on approaches adequately accounting for both factors. For this reason, we compute the spin-projected resistivities as functions of x and y in $Mn_{3-x}X_xGa$, $Mn_{3-y}Y_yGa$, and $Mn_{3-x-y}X_xY_yGa$ alloys in the following, using the Kubo-Greenwood linear-response formalism [31,32] and applying the relativistic spin-projection scheme [34].

D. Quantitative analysis of spin polarization

Since we examined the tetragonal systems, we will distinguish their properties along the in-plane (xy, or the ab plane of the tetragonal lattice) and out-of-plane (along z, or the c axis of the tetragonal lattice) directions. Figures 3(a) and 3(c) represent the in-plane transport properties (spin-projected resistivities and spin polarizations, respectively), whereas Figs. 3(b) and 3(d) represent the out-of-plane characteristics. In all cases, we assume that M is oriented along the z axis because of the magnetocrystalline anisotropy. Here, we consider the diagonal elements of the resistivity tensor, $\rho_{xx} = \rho_{yy} \neq \rho_{zz}$, as being responsible for the direct current, $\vec{j}$ ($j_\alpha = E_\alpha/\rho_{\alpha\alpha}$, $\vec{E}$ is the external electric field, and α is the spatial index x, y, or z). The corresponding spatial components of spin polarization are defined as $P_{\alpha\alpha} = \frac{\rho_{\alpha\alpha}^\downarrow - \rho_{\alpha\alpha}^\uparrow}{\rho_{\alpha\alpha}^\downarrow + \rho_{\alpha\alpha}^\uparrow}$, where $\rho_{\alpha\alpha}^{\uparrow,\downarrow}$ are the corresponding spin projections.

As follows from Figs. 3(a) and 3(b), with increasing chemical disorder induced by Mn-X or Mn-Y substitution, almost all spatial/spin resistivity components grow monotonously within $0 \leqslant x, y \leqslant 0.5$ (with very few exceptions, e.g., for $\rho_{xx}^\uparrow$ in the case of $X =$ Sc and Ti at higher x rates, due to a certain increase in $n_F^\uparrow$). This growth is most efficient for small x or y, and it tends to saturate close to $x \approx y \approx 0.5$ (maximal disorder). For the ordered Mn_3Ga, all resistivity components are exactly zero; for this reason, we estimate its spin polarization by extrapolating corresponding expressions to $x, y \to 0$. Here, we find that the pure Mn_3Ga represents a rather large spin-polarization
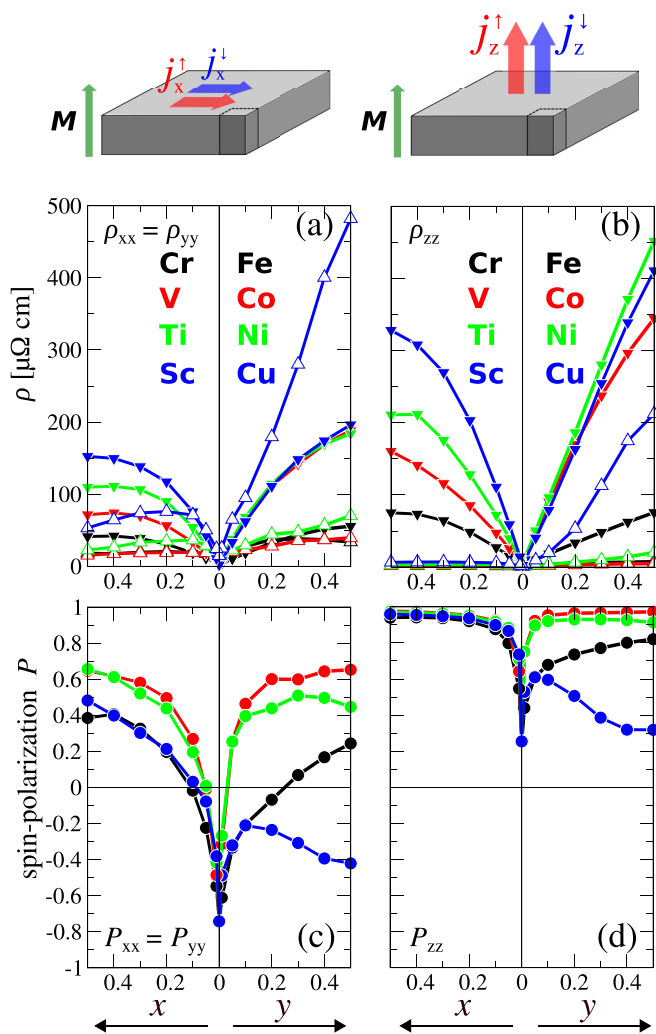

FIG. 3. (Color online) Spatial components of residual resistivities, $\rho_{xx} = \rho_{yy}$ (a) and ρ_{zz} (b) (their spin projections, $\rho^{\uparrow(\downarrow)}$, are distinguished by the hollow up- and filled down-oriented triangles), computed as functions of $Mn_{1-y}Y_y$ ($Y =$ Fe, Co, Ni, Cu) and $Mn_{1-x}X_x$ ($X =$ Cr, V, Ti, Sc) random substitutions; the substitution rates x and y increase in the directions indicated by the arrows. Spatial components of spin polarization, $P_{xx} = P_{yy}$ (c) and P_{zz} (d), are derived from the spin projections of the corresponding residual resistivity spatial components. The corresponding schemes with electric current, $\vec{j}$, magnetization, $\vec{M}$, and the unit-cell relative orientations are shown above.

spatial anisotropy: $P_{xx} = P_{yy} \approx -0.75$ [Fig. 3(c)], whereas $P_{zz} \approx +0.25$ [Fig. 3(d)], which indicates that the spin-polarization estimates for anisotropic systems (e.g., [22]) based on a spin-resolved DOS at E_F can be improved by considering the spatially resolved DOS in momentum space. The resistivity spin component trends as functions of x and y show that $\rho^\downarrow$ grows faster than $\rho^\uparrow$, which essentially justifies the proposed scheme (see Sec. II). Indeed, both P_{xx} and P_{zz}, as functions of x or y, evolve toward larger positive values. The absolute disorder-induced change of the P_{xx} component is very large, from -0.75 to approximately $+0.65$ (for Mn-Ti, Mn-V, and Mn-Co substitutions), i.e., $\Delta P_{xx} \approx 1.4$. Despite the fact that this particular effect is not especially interesting,

since absolute spin polarization does not increase, it clearly demonstrates the importance of disorder.

An interesting point worth mentioning is that the disorder influence is stronger for those alloys in which the substituting type (X or Y) is further from Mn (e.g., in terms of the group or valence electrons number), i.e., a larger potential difference leads to a stronger random fluctuation amplitude. Indeed, for the types "closest" to Mn, i.e., $X =$ Cr and $Y =$ Fe, the corresponding resistivity components are comparably small (e.g., at $x = y = 0.5$): $\rho_{xx}^{\uparrow}$: $18 \sim 33$, $\rho_{xx}^{\downarrow}$: $41 \sim 55$, $\rho_{zz}^{\uparrow}$: $2.3 \sim 7.5$, and $\rho_{zz}^{\downarrow}$: $75.3 \sim 75.7$ $\mu\Omega$ cm. At the same

time, for the types "most distinct" from Mn, i.e., $X =$ Sc and $Y =$ Cu, certain resistivity components are much larger, but not always comparable: $\rho_{xx}^{\uparrow}$: $53 \approx 481$, $\rho_{xx}^{\downarrow}$: $152 \sim 197$, $\rho_{zz}^{\uparrow}$: $6.9 \approx 212$, and $\rho_{zz}^{\uparrow}$: $327 \sim 411$ $\mu\Omega$ cm. This simply indicates that, whereas substitution of Mn with "too similar" elements is not yet appropriately efficient, substitution with "too distinct" elements rapidly escapes control, since the band structure is strongly affected not only in the sense of the Bloch-wave broadening, but also in the sense of dispersion, E_F position, etc. The most inefficient situation is observed for Mn-Cu substitution. Here, $\rho^{\uparrow}$ and $\rho^{\downarrow}$ grow rapidly by
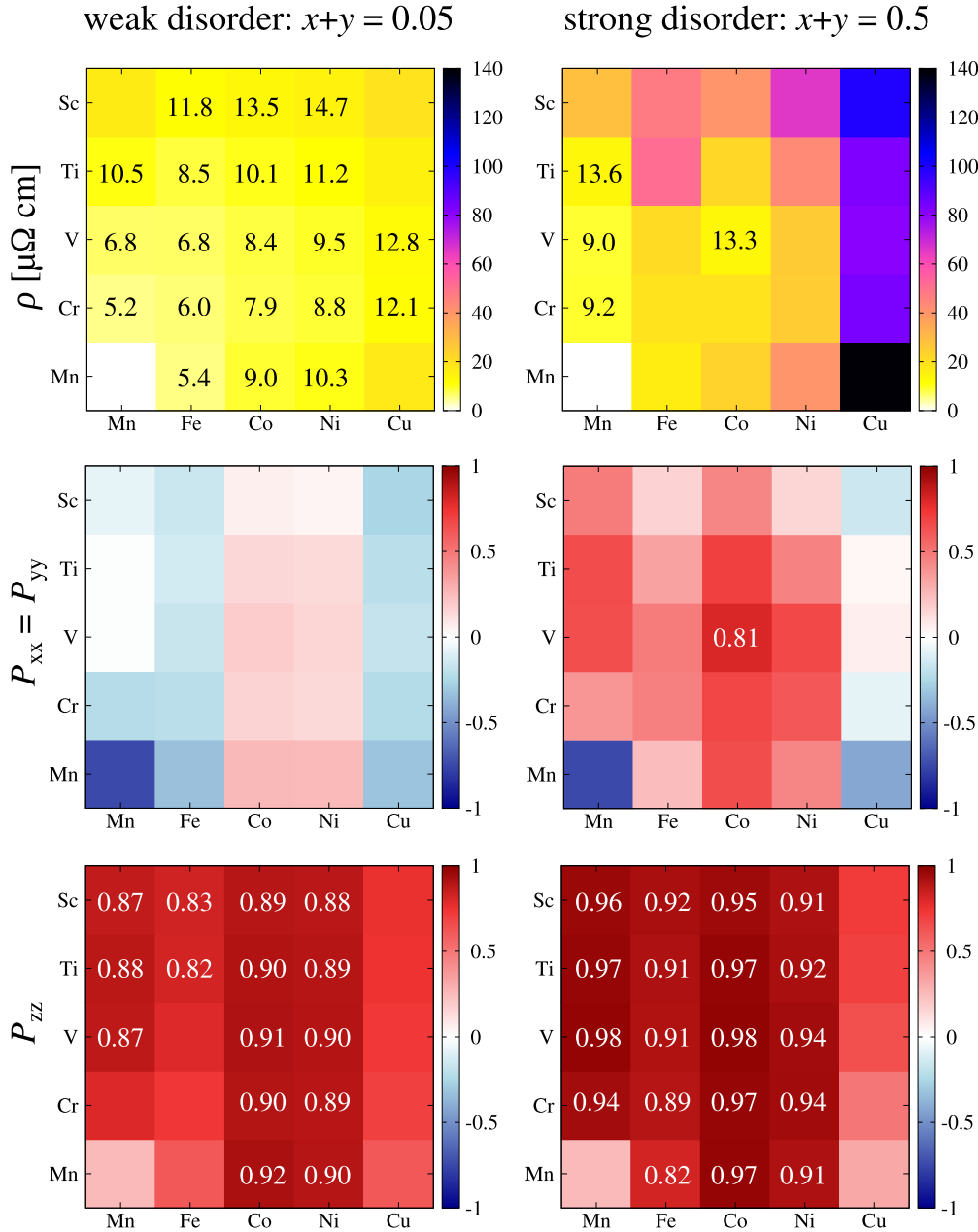

FIG. 4. (Color online) Residual resistivities, ρ (averaged over spins and spatial directions) and spin-polarization spatial components ($P_{xx} = P_{yy}$, within the xy plane; P_{zz}, out-of-plane) calculated for $Mn_{3-x-y}X_xY_y$ compositions ($X =$ Cr, V, Ti, Sc; $Y =$ Fe, Co, Ni, Cu; formally, we also include Mn). The total amount of substituted Mn is fixed to either $x + y = 0.05$ (weak disorder, left side) or to $x + y = 0.5$ (strong disorder, right side). Thus, for the strong disorder, if, for example, $x = 0$, then $y = 0.5$, and vice versa, or if both $x, y > 0$, then $x = y = 0.25$. For the compositions with $P > 0.8$ and $\rho < 15$ $\mu\Omega$ cm, the corresponding values are shown explicitly.

achieving large absolute values, but their ratios, and thus the spin polarization, remain unsatisfactorily low. In contrast, substitution with "intermediate" elements, $X = V$, Ti, or $Y = $ Co, Ni, appears to be very efficient. Specifically, at $x, y \approx 0.1$ the out-of-plane spin polarization achieves $P_{zz} \approx 0.91$–0.95 and grows further with increased disorder rate. As follows from Fig. 3(b), such growth is mainly due to the increase of the $\rho_{zz}^{\downarrow}$ component, whereas $\rho_{zz}^{\uparrow}$ remains almost unaffected, as was supposed in Sec. II during the discussion of the constructive disorder design.

To also study the combined effects (in $\mathrm{Mn}_{3-x-y}X_xY_y$ compositions), we plot the computed transport characteristics, $P_{xx} = P_{yy}$ and P_{zz}, together with the spatially averaged and spin-averaged (effective) resistivity, $\rho = (2\rho_{xx} + \rho_{zz})/3$, where $\rho_{\alpha\alpha} = 1/\left(1/\rho_{\alpha\alpha}^{\uparrow} + 1/\rho_{\alpha\alpha}^{\downarrow}\right)$ is computed for the weak $(x + y = 0.05)$ and strong $(x + y = 0.5)$ disorder regimes, as shown in Fig. 4. It can be seen that, by moving toward Sc and Cu, the effective resistivity tends to increase. In both disorder regimes this larger resistivity is exhibited by all Cu-containing compositions, with a maximum of approximately 140 $\mu\Omega$ cm for the $\mathrm{Mn}_{2.5}\mathrm{Cu}_{0.5}\mathrm{Ga}$ alloy. At the same time, the spin polarization of metals with large resistivity is always low, since the spin component with higher resistivity cannot go far beyond the Mooij limit, whereas the other spin component with lower resistivity is already sufficiently high. On the other hand, alloys with lower effective resistivities, such as Co- or V-containing compositions, exhibit much higher spin polarization. Interestingly, they show a noticeable "complementary" effect, seen, for example, in the strongly disordered regime; whereas for both $\mathrm{Mn}_{2.5}\mathrm{Co}_{0.5}\mathrm{Ga}$ and $\mathrm{Mn}_{2.5}\mathrm{V}_{0.5}\mathrm{Ga}$, $P_{xx} \approx 0.65$, for the combined composition, $\mathrm{Mn}_{2.5}\mathrm{V}_{0.25}\mathrm{Co}_{0.25}\mathrm{Ga}$, it is already 0.81. It is also instructive to admit the efficiency of the constructive disorder; by moving from $\mathrm{Mn}_3\mathrm{Ga}$ through the weakly disordered $\mathrm{Mn}_{2.95}\mathrm{V}_{0.025}\mathrm{Co}_{0.025}\mathrm{Ga}$ to $\mathrm{Mn}_{2.5}\mathrm{V}_{0.25}\mathrm{Co}_{0.25}\mathrm{Ga}$, which is ten times more strongly disordered, P_{zz} evolves from 0.25 through 0.91 to 0.98, respectively. This means that, in order to achieve high spin polarization, the small substitution rate is already sufficient.

IV. SUMMARY AND OUTLOOK

As we have seen, an increase in spin polarization is observed almost for any type of Mn-TM substitution within $\mathrm{Mn}_3\mathrm{Ga}$, beginning with Sc and ending with Ni. The exception is the Mn-Cu case, which leads to a very strong random potential fluctuation affecting both spin channels. The important feature of $\mathrm{Mn}_3\mathrm{Ga}$ is its tetragonal structure, which causes a large anisotropy in its transport characteristics. As a result, the spin polarization along the in-plane and out-of-plane directions evolves differently. Whereas the disorder-induced change is strong in both directions, it is the most constructive in the out-of-plane direction only. At the same time, the constructive effect is achieved immediately by beginning with a small Mn-TM substitution rate. This is suitable for spintronics elements exploiting magnetoresistance effects, as the unnecessarily high resistance of the electrodes produces unwanted energy losses. Another positive aspect of the presented scheme is the improvement in spin polarization specifically for the "current-perpendicular-to-plane" (CPP) setup. This improvement in combination with perpendicular magnetic anisotropy

is applicable to many state-of-the-art industrial developments. On the other hand, this also means that the direct experimental proof of the proposed scheme, at least on a $\mathrm{Mn}_3\mathrm{Ga}$ basis, requires preparation of the single-crystalline structures with effective stoichiometric control, which is rather sophisticated. In this respect, an interesting future focus is constructive disorder design in cubic systems, as high spin polarization can be expected in the isotropic case even for polycrystalline materials. As we have seen, the basic feature that provides the necessary conditions for such disorder engineering is the presence of two antiparallel magnetic sublattices. Hence, suitable cubic candidates for this research can be found within the same Mn-rich Heusler group.

APPENDIX

Here we present the first-principles justification of the chemical ordering rules used to model the Heusler materials in Sec. II and discussed in Sec. III B [see assumption (ii)]. To distinguish between different chemical orders within the same composition, we will note them according to the sequence of Wyckoff positions, $2a$ $2b$ $2c$ $2d$ (also see the caption of Fig. 1). For example, $[\mathrm{Mn}_{1-x}X_x]\mathrm{GaMn}$ and $\mathrm{MnGaMn}[\mathrm{Mn}_{1-x}X_x]$ configurations are distinguished by the position of the X element, which occupies $2a$ Wyckoff site in the first case, and $2d$ in the second case, respectively.

As it follows from the calculations shown in Fig. 5, for the compositions containing early TMs ($X = $ Cr, V, Ti, and Sc), the total energy difference, defined as $\Delta E = E_{[\mathrm{Mn}_{1-x}X_x]\mathrm{GaMnMn}} - E_{\mathrm{MnGaMn}[\mathrm{Mn}_{1-x}X_x]}$, appears to be negative within the whole range, $0 < x < 0.5$. This indicates that the
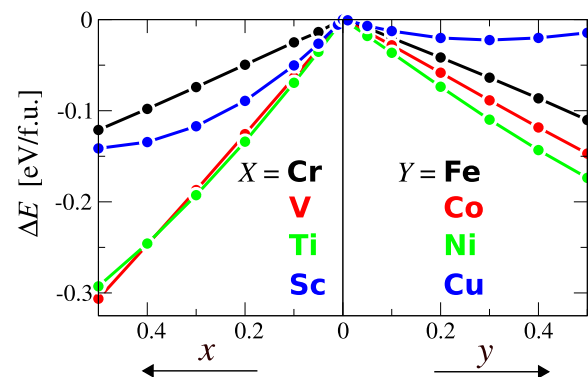

FIG. 5. (Color online) Total energy difference per formula unit ΔE between two configurations of the same Mn-TM Ga composition (for more details, see the text) calculated as a function of the substitution rate for $\mathrm{Mn}_{1-x}X_x$ (left, $X = $ Cr, V, Ti, Sc; $0 < x < 0.5$), and $\mathrm{Mn}_{1-y}Y_y$ (right, $Y = $ Fe, Co, Ni, Cu; $0 < y < 0.5$). The substitution rates x and y increase along the directions indicated by arrows. The data and the legends correspond to the same color code (as was introduced in Fig. 3).

earlier TM will substitute Mn preferentially on the $2a$ Wyckoff site, rather than on $2c$ or $2d$. In the case of late TM substitutions ($Y = $ Fe, Co, Ni, and Cu), the total energy difference, defined as $\Delta E = E_{\text{MnGaMn}[\text{Mn}_{1-y}Y_y]} - E_{[\text{Mn}_{1-y}Y_y]\text{GaMnMn}}$, appears to be also negative within the whole substitution range. Thus, the later TM will substitute Mn preferentially on $2c/2d$ Wyckoff sites, rather than on $2a$.

By assuming a linear behavior of ΔE upon x or y, it follows that the occupation of the "wrong" Wyckoff site costs such a huge amount of energy that it can be easily identified by even more rough estimations (from about 0.04 eV for Cu to 0.6 eV for V or Ti). This also indicates the general validity of these rules for those Heusler materials that are known experimentally. Here we do not consider more delicate situations, such as, e.g., distinguishing between MnGaMn[Mn$_{1-y}Y_y$] and, say, MnGa[Mn$_{1-y/2}Y_{y/2}$][Mn$_{1-y/2}Y_{y/2}$] configurations, since their energy differences are smaller by at least by one order of magnitude, and thus their properties must be rather similar. In addition, those experiments that claim to distinguish between the centrosymmetric and the noncentrosymmetric point groups using x-ray diffraction all indicate the absence of inversion symmetry for Mn$_{3-y}Y_y$ MG compositions (where Y is the late TM, and the MG is the main-group element, i.e., not only Ga). Hence, in order to consider more complicated chemical configurations, we need to have an important experimental precedent, as in the case of Fe$_2$-based Heusler materials [35,36].

For the combined compositions, such as Mn$_{3-x-y}X_xY_y$Ga, one can easily show in the same fashion (we do not present the corresponding total energies just to prevent a large amount of unnecessary data) that the lowest energy configurations are again those that contain the earliest TM atom X in $2a$ and the latest TM atom Y on $2c$ or $2d$. The corresponding total energy differences between the lowest- and the higher-energy configurations can be closely described by linear combinations of the total energies of the corresponding single-element Mn$_{3-x}X_x$Ga and Mn$_{3-y}Y_y$Ga substitutions.

[1] W. F. Smith and J. Hashemi, *Foundations of Materials Science and Engineering*, 3rd ed. (McGraw-Hill, New York, 2004).

[2] J. Pierre, B. Dollet, and V. Leroy, Phys. Rev. Lett. **112**, 148307 (2014).

[3] L. Sapienza, H. Thyrrestrup, S. Stobbe, P. D. Garcia, S. Smolka, and P. Lodahl, Science **327**, 1352 (2010).

[4] P. W. Anderson, Phys. Rev. **109**, 1492 (1958).

[5] D. J. Thouless, Phys. Rep. C **13**, 93 (1974).

[6] J. Li, R.-L. Chu, J. K. Jain, and S.-Q. Shen, Phys. Rev. Lett. **102**, 136806 (2009).

[7] C. W. Groth, M. Wimmer, A. R. Akhmerov, J. Tworzydło, and C. W. J. Beenakker, Phys. Rev. Lett. **103**, 196805 (2009).

[8] H. Jiang, L. Wang, Q.-F. Sun, and X. C. Xie, Phys. Rev. B **80**, 165316 (2009).

[9] N. Mott, Proc. R. Soc. London, Ser. A **153**, 699 (1936).

[10] J. H. Mooij, Phys. Status Solidi A **17**, 521 (1973).

[11] J. Kübler, A. R. Williams, and C. B. Sommers, Phys. Rev. B **28**, 1745 (1983).

[12] R. A. de Groot, F. M. Mueller, P. G. van Engen, and K. H. J. Buschow, Phys. Rev. Lett. **50**, 2024 (1983).

[13] P. Soven, Phys. Rev. **156**, 809 (1967).

[14] D. W. Taylor, Phys. Rev. **156**, 1017 (1967).

[15] W. H. Butler, Phys. Rev. B **31**, 3260 (1985).

[16] W. Metzner and D. Vollhardt, Phys. Rev. Lett. **62**, 324 (1989).

[17] G. Kotliar, S. Y. Savrasov, K. Haule, V. S. Oudovenko, O. Parcolett, and C. A. Marianetti, Rev. Mod. Phys. **78**, 865 (2006).

[18] S. Chadov, G. H. Fecher, C. Felser, J. Minár, J. Braun, and H. Ebert, J. Phys. D **42**, 084002 (2009).

[19] J.-P. Wüstenberg, R. Fetzer, M. Aeschlimann, M. Cinchetti, J. Minár, J. Braun, H. Ebert, T. Ishikawa, T. Uemura, and M. Yamamoto, Phys. Rev. B **85**, 064407 (2012).

[20] M. Jourdan, J. Minár, J. Braun, A. Kronenberg, S. Chadov, B. Balke, A. Gloskovskii, M. Kolbe, H. J. Elmers, G. Schönhense *et al.*, Nat. Commun. **5**, 3974 (2014).

[21] P. J. Webster, Contemp. Phys. **10**, 559 (1969).

[22] J. Winterlik, B. Balke, G. H. Fecher, C. Felser, M. C. M. Alves, F. Bernardi, and J. Morais, Phys. Rev. B **77**, 054406 (2008).

[23] V. Alijani, J. Winterlik, G. H. Fecher, and C. Felser, Appl. Phys. Lett. **99**, 222510 (2011).

[24] J. Winterlik, S. Chadov, A. Gupta, V. Alijani, T. Gasi, K. Filsinger, B. Balke, G. H. Fecher, C. A. Jenkins, F. Casper *et al.*, Adv. Mater. **24**, 6283 (2012).

[25] K. Rode, N. Baadji, D. Betto, Y.-C. Lau, H. Kurt, M. Venkatesan, P. Stamenov, S. Sanvito, J. M. D. Coey, E. Fonda *et al.*, Phys. Rev. B **87**, 184429 (2013).

[26] P. W. Anderson, Phys. Rev. **124**, 41 (1961).

[27] H. Ebert, D. Ködderitzsch, and J. Minár, Rep. Prog. Phys. **74**, 096501 (2011).

[28] J. P. Perdew, K. Burke, and M. Ernzerhof, Phys. Rev. Lett. **77**, 3865 (1996).

[29] A. Perlov, A. Yaresko, and V. Antonov (unpublished).

[30] O. Meshcheriakova, S. Chadov, A. K. Nayak, U. K. Rössler, J. Kübler, G. André, A. A. Tsirlin, J. Kiss, S. Hausdorf, A. Kalache *et al.*, Phys. Rev. Lett. **113**, 087203 (2014).

[31] R. Kubo, J. Phys. Soc. Jpn. **12**, 570 (1957).

[32] D. A. Greenwood, Proc. Phys. Soc. **71**, 585 (1958).

[33] B. Velický, Phys. Rev. **184**, 614 (1969).

[34] S. Lowitzer, D. Ködderitzsch, and H. Ebert, Phys. Rev. B **82**, 140402(R) (2010).

[35] T. Gasi, V. Ksenofontov, J. Kiss, S. Chadov, A. K. Nayak, M. Nicklas, J. Winterlik, M. Schwall, P. Klaer, P. Adler *et al.*, Phys. Rev. B **87**, 064411 (2013).

[36] J. Kiss, S. Chadov, G. H. Fecher, and C. Felser, Phys. Rev. B **87**, 224403 (2013).